energies

Article

Quasi-Periodic Harmonic Feature Extraction of Power Signals via Improved Scaling-Basis Chirplet Transform

Yihao Hu * and Jiexiao Yu *

School of Electrical and Information Engineering, Tianjin University, Tianjin 300072, China
* Correspondence: 2023234009@tju.edu.cn (Y.H.); yjx@tju.edu.cn (J.Y.); Tel.: +86-17302219187 (Y.H.)

Abstract

The increasing randomness of source–load fluctuations and the rapid proliferation of power-electronic devices have introduced wide dynamic ranges, fast time-varying behaviors, and strong stochastic characteristics into power signals, leading to severe measurement deviations in existing metering equipment. Conventional modeling and feature analysis methods based on fixed-frequency steady-state assumptions are inadequate for characterizing such non-stationary behaviors, making the underlying causes of metering deviations difficult to identify. To address this issue, we propose a modeling and dynamic time–frequency feature extraction method for complex non-stationary power signals. First, the operating characteristics of power equipment are analyzed to identify the fundamental non-stationary features of power signals, based on which a quasi-periodic harmonic signal model is established. Then, the scaling-basis chirplet transform is employed to intuitively represent the time–frequency structure, while a ridge detection algorithm is incorporated to quantitatively characterize the time–frequency trajectories and instantaneous amplitude features. Finally, to cope with the limited availability of power signal measurements, a non-stationary component reconstruction method based on cross-correntropy is developed. Experimental results from multiple datasets, including field-measured signals, demonstrate that the proposed method enables effective dynamic monitoring and reconstruction of non-stationary components, offering significant advantages in both time–frequency analysis capabilities and reconstruction accuracy.

Keywords: non-stationary signal; power metering; chirplet transform; time–frequency analysis; cross-correntropy

Academic Editor: Juan-José González de la Rosa

Received: 11 March 2026
Revised: 21 April 2026
Accepted: 24 April 2026
Published: 28 April 2026

1. Introduction

With the development of modern power systems, the penetration of renewable energy sources such as solar and wind power has increased rapidly. While facilitating the transition toward clean and low-carbon energy, this trend has also significantly intensified the stochastic characteristics of electrical signals. The widespread deployment of power-electronic devices on the user side introduces pronounced nonlinear fluctuations into power signals, which can be further amplified by grid resonances, thereby enhancing transient and interharmonic disturbances [1,2].

Consequently, the intermittent and fluctuating power outputs of renewable energy sources, together with the high-speed switching operating modes of power-electronic equipment, cause electrical signals (i.e., voltage and current) to exhibit persistent fundamental-frequency dynamics, wide-range variations, harmonic reactive components, and broadband spectral characteristics at the macroscopic level [3,4]. These features render power signals inherently random, time-varying, and non-stationary. Conventional analysis methods based on fundamental components and higher-order harmonic indices are insufficient to provide an effective mathematical representation of such behaviors. Moreover, the wide dynamic range, fast time-varying nature, and strong randomness of these signals may lead to measurement deviations in existing power metering devices, particularly when confronted with rapid fluctuations occurring within fewer than ten fundamental cycles [5–7]. Such metering deviations are most prominent in the key deployment scenarios of modern power systems, including distributed renewable generation and emerging flexible loads, and are directly associated with system stability, as well as the operational efficiency of upstream and downstream stakeholders in power infrastructure. Therefore, the investigation and analysis of random non-stationary components in complex power signals are of great significance.

At present, most mathematical modeling approaches for power signals are developed within the framework of classical harmonic models. Wang et al. modeled complex power signals as harmonic signals whose amplitudes follow binary keying modulation in [8]. Yang et al. represented supraharmonic components as harmonic signals with exponentially decaying amplitudes in [9]. Sun et al. proposed a multi-source harmonic coupling modeling method in [10]. Although these models exhibit different characteristics, they all fundamentally rely on fixed-frequency steady-state assumptions, which makes them difficult to adapt to the wide dynamic range, fast time-varying behavior, and strong randomness exhibited by modern power signals.

To describe signal dynamics, time–frequency representation methods, which jointly characterize signals in the time and frequency domains, have been widely recognized as effective tools for non-stationary signal analysis. Common time–frequency techniques, such as short-time Fourier transform (STFT), wavelet transform (WT), and Wigner–Ville distribution, have been applied to various signal feature analysis tasks [11–15]. However, these conventional time–frequency analysis methods are inherently limited by the time–frequency uncertainty principle, the use of fixed basis functions, and cross-term interference. These limitations make them inadequate for accurately characterizing the wide dynamic range, fast time-varying behavior, and strong randomness of power signals.

Existing improvement approaches can be broadly categorized into three groups: adaptive transforms (e.g., ASTFT [16] and PWVD [17]), post-processing methods (e.g., SST [18] and MSST [19]), and chirplet-based analysis methods. In power signal analysis, adaptive and post-processing methods still heavily rely on the quality of the initial time–frequency representation. When strong random perturbations or rapid frequency variations are present, their performance improvement is often limited.

Chirplet-based methods attempt to address these issues by introducing frequency-modulated basis functions to better match signal structures. The classical chirplet transform (CT) [20] aligns the chirp rate with the instantaneous frequency trajectory, which is effective for linear frequency-modulated signals. However, since it assumes a constant chirp rate, it cannot adequately capture continuously drifting frequencies and rapidly time-varying characteristics in power signals, leading to clear limitations in complex non-stationary scenarios.

To overcome this drawback, several improved methods, such as the polynomial chirplet transform (PCT) [21] and the spline–kernel chirplet transform (SCT) [22], introduce time-varying chirp rates to enhance the modeling of nonlinear frequency variations. Nevertheless, under the multicomponent coupling conditions commonly observed in power signals, these methods still struggle to simultaneously match multiple frequency trajectories. In addition, their parameter estimation typically relies on iterative optimization, which increases computational complexity and reduces robustness in the presence of strong noise and random disturbances.

Further extensions, including GLCT [23], VSLCT [24], HOCT [25], and EALCT [26], attempt to address multicomponent and nonlinear characteristics through parameter fusion, post-processing, or adaptive basis construction. However, in practical power signal analysis, these methods still exhibit strong dependence on prior information, sensitivity to closely spaced frequency components, and insufficient energy concentration under noisy conditions. As a result, spectral overlap and time–frequency blurring are prone to occur, especially when components are strongly coupled or have small frequency spacing.

To address these challenges, we have investigated and proposed a quasi-periodic dynamic time–frequency analysis and non-stationary feature extraction method for power signals based on an improved scaling-basis chirplet transform. First, starting from the operating mechanisms of power-electronic equipment, the following formation mechanisms are analyzed: wide dynamic range, fast time-varying behavior, and strong randomness in power signals. On this basis, a dynamic adaptive time-varying signal model is constructed to mathematically characterize random time-varying frequency shifts and high-frequency transient amplitude variations. Second, an improved scaling-basis chirplet transform with four adjustable degrees of freedom, namely time delay, scale, chirp rate, and center frequency, is developed to achieve high-resolution time–frequency representation of non-stationary signals. By also incorporating a ridge detection algorithm, the time–frequency trajectories and instantaneous amplitude features of individual signal components are accurately extracted. Finally, the extracted time–frequency trajectories and instantaneous amplitude features are utilized to separate and reconstruct target components.

2. Materials and Methods

2.1. Operating Characteristics Analysis of Power-Electronic Electrical Equipment

This study first analyzes the formation mechanisms of the wide dynamic range, fast time-varying behavior, and strong randomness in power signals from the operating principles of power-electronic equipment. Specifically, nonlinear devices such as power-electronic converters inject discrete spectral components and continuous spectral components with random time-varying frequency shifts into the power grid during operation, thereby introducing pronounced random time-varying frequency-shift characteristics into power signals.

A typical time-domain waveform of a random time-varying frequency shift is illustrated in Figure 1. Figure 2 presents the time–frequency representation of the waveform shown in Figure 1.

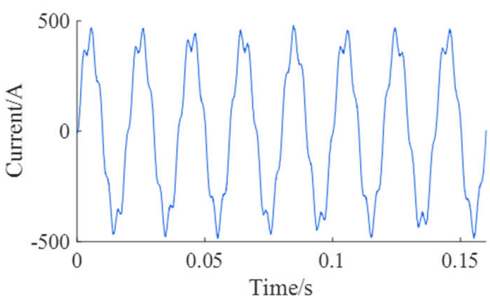

Figure 1. Recorded waveform of a time-varying frequency-shift signal from a wind farm.

Conventional harmonic metering methods are established under fixed-frequency steady-state assumptions; they cannot accurately represent random time-varying frequency shifts characterized by the superposition of discrete and continuous spectra owing to discrete and continuous spectral characteristics, as well as inherent time-varying behavior. To elucidate the underlying mechanism, we decompose the evolution process into two stages: discrete injection and continuous spectral broadening:

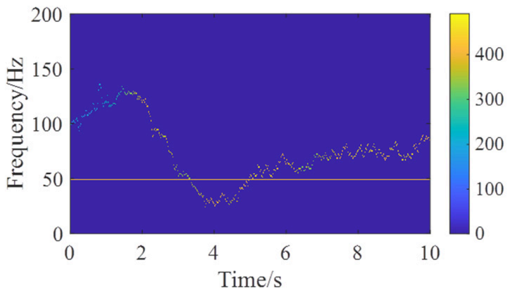

Figure 2. Time–frequency representation corresponding to the waveform in Figure 1.

In the first stage, characteristic harmonics generated by p-pulse rectifiers or periodic power disturbances originating from the source side of renewable energy systems inject discrete spectral components into the power system. The corresponding set of frequencies can be expressed as

$$\Phi = \{f | f = (np+1)f_g, n \in \mathrm{N}^+\} \cup \{f | f = kf_g \pm f_{dc}, k \in \mathrm{Z}\} \tag{1}$$

where f_g denotes the grid fundamental frequency, p represents the pulse number, and f_{dc} denotes the frequency of power disturbances on the source side of renewable energy systems.

In the second stage, the discrete spectral components are spread into continuous spectral components due to the stochastic PWM control strategies of converters, as well as the finite bandwidth and inherent time delay of closed-loop control systems.

(1) The original signal in the system containing discrete spectral components can be expressed as the superposition of a set of discrete spectral lines,

$$x_0(t) = \sum_i A_i \cos(2\pi f_i t), f_i \in \Phi \tag{2}$$

but the carrier frequency of stochastic PWM is no longer fixed at a constant value.

$$f_c(t) = \overline{f}_c + \Delta f(t) \tag{3}$$

Thus, the corresponding signal can be written as

$$x(t) = \sum_i A_i \cos(2\pi f_i t + \psi_i(t)), f_i \in \Phi \tag{4}$$

$$\psi_i(t) = 2\pi \int_0^t \Delta f(\tau) d\tau \tag{5}$$

(2) The transfer function of the converter closed-loop control system can be expressed as

$$F(s) = \frac{e^{-s\tau_d}}{1 + L(s)} \tag{6}$$

where τ_d denotes the time delay, and $L(s)$ represents the open-loop transfer function of the control loop.

Meanwhile, when the converter is subjected to an external disturbance, d(t), the signal in (2) can be expressed, after a first-order small-signal expansion, as

$$x(t) = \sum_i A_k \cos(2\pi f_k t - \Delta\phi_k(t)) \tag{7}$$

$$\Delta\phi_k(t) = \mathcal{L}^{-1}\left\{ \frac{1}{1 + L(s)} d(t) - \frac{L(s)}{1 + L(s)} n(t) \right\} \tag{8}$$

https://doi.org/10.3390/en19092122

where $n(t)$ denotes the system measurement noise, and $\mathcal{L}^{-1}$ represents the inverse Laplace transform. (7) and (8) show that discrete spectral components broaden into continuous spectral components after passing through the converter.

In high-frequency transient amplitude variation, the amplitude of power signals in modern power systems exhibits high-frequency fluctuations, a wide variation range, and rapid variation rates, as illustrated in Figure 3. This behavior mainly manifests in the following two typical forms.

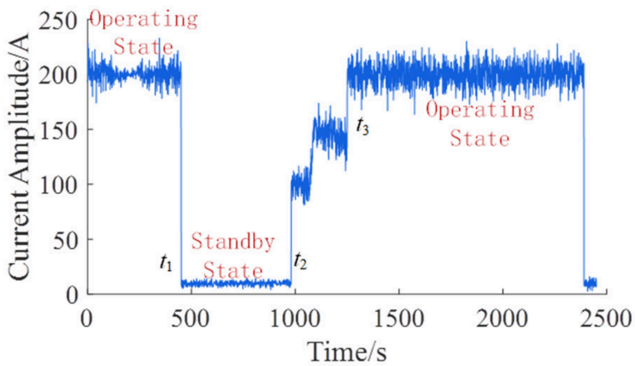

Figure 3. Amplitude waveform of the current signal from a high-power nonlinear device.

(1) Mean-value migration can be induced by operating condition switching in the high-power equipment, which is characterized by a large step-like jump in signal amplitude occurring within an extremely short time interval.

$$A(t) = A_0 + \frac{\Delta A}{\Delta t} \cdot u(t - t_1)u(t - t_1 + \Delta t) \tag{9}$$

where ΔA denotes the amplitude jump, t_1 represents the onset time of the transition, Δt denotes the duration of the transition, and A_0 represents the amplitude before the transition.

As shown in Figure 4, when a certain device switches from an operating state to a standby state, the fluctuation range can reach as high as 200 A within 0.08 s, corresponding to an extremely high temporal slope of 2500 A/s.

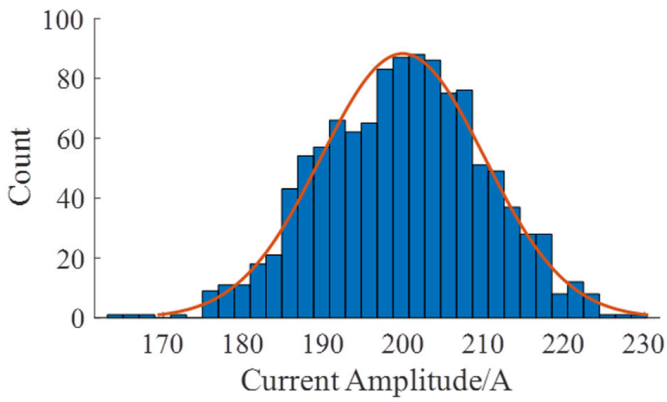

Figure 4. Histogram of amplitude distribution (taking the time interval t_2–t_3 in Figure 3 as an example).

(2) High-frequency fluctuations can occur under a given operating condition, where the signal amplitude exhibits frequent oscillations around the mean value corresponding to that operating condition across different equipment states. As shown in Figure 3, the variation pattern can be approximately characterized by a normal distribution. As shown

in Figure 4, the histogram of amplitude distribution is presented by taking the time interval t_2–t_3 in Figure 3 as an example.

$$A(t) \sim N(A_3, \delta^2), t_3 < t < t_4 \tag{10}$$

where A_3 denotes the mean value over the time interval t_2–t_3, and δ_2 represents the variance.

Notably, when a device undergoing rapid operating-condition transitions simultaneously acts as a harmonic source injecting random time-varying frequency-shift components into the power grid, the resulting high-frequency transient amplitude variations are not limited to the fundamental component. Instead, the amplitudes of the injected frequency-shift components also exhibit instantaneous variations.

Moreover, in practical modern power systems, power signals are often formed through the superposition of multiple components driven by different disturbance sources, each of which may contain time-varying frequency shifts and transient amplitude variations. Consequently, these signals exhibit pronounced multi-component coupling characteristics.

Therefore, power signals in modern power systems present fast dynamics and rapidly time-varying behaviors, constituting strongly non-stationary quasi-periodic harmonic signals that are distinctly different from conventional random signals and chaotic signals. Quasi-periodic harmonic components lead to severe deviations in traditional power metering methods. Hence, it is necessary to model, analyze, and extract the features of these components to investigate the underlying mechanisms of metering deviations.

2.2. Quasi-Periodic Harmonic Signal Model

Based on the analysis presented in Section 1, the following demonstrates how the traditional harmonic model can be improved in accordance with the characteristics of quasi-periodic harmonic signals. Conventional power signal modeling approaches still adopt the classical harmonic modeling framework, expressed as follows:

$$G(t) = a_0 + h_i(t) = a_0 + \sum_{i=1}^{K} a_i \cos(2\pi t \cdot 50i) \tag{11}$$

It is evident that $G(t)$ denotes the superposition of harmonic components h_i(t) = a_i cos(2πt × 50i) with frequencies equal to 50i, where i = 1, 2, . . ., K. As discussed in the previous section, many devices in modern power systems introduce non-fundamental-frequency components with dynamically time-varying frequencies into power signals. These components include both discrete spectral components and continuous spectral components. To enable the model to simultaneously represent discrete and continuous spectral components, the harmonic term, $h_\mathrm{i}(t)$, in (11) is replaced by the expression in (12).

$$h_i(t) = a_i \cos(2\pi * \Psi_i(t)) \tag{12}$$

Definition 1. *The instantaneous frequency of a signal component, $h_i(t)$, expressed as (12), is defined as the time derivative of its phase function, $\Psi_i(t)$; that is,*

$$f_i(t) = \frac{d\Psi_i(t)}{dt} \tag{13}$$

Then, $f_i(t)$ is referred to as the instantaneous frequency of component $h_i(t)$.

Definition 2. *A time–frequency trajectory refers to a single-valued curve formed by the instantaneous frequency varying with time, which is an important feature for characterizing the temporal evolution of a signal.*

To accurately characterize high-frequency transient amplitude variations, the constant coefficient ai is replaced by the instantaneous amplitude, $A_i(t)$, as shown in (14).

$$h_i(t) = A_i(t)\cos(2\pi * \Psi_i(t)) \tag{14}$$

Definition 3. *The instantaneous amplitude refers to the amplitude of a signal component, $h_i(t)$, when it is expressed as (14). In this case, $A_i(t)$ is defined as the instantaneous amplitude of component $h_i(t)$.*

Definition 4. *An instantaneous amplitude profile refers to a single-valued curve describing the variation in instantaneous amplitude with time and is also an important feature for characterizing the temporal evolution of a signal.*

To extract the time–frequency trajectory and instantaneous amplitude profile of component $h_i(t)$, it is necessary to introduce the concept of the analytic signal.

Definition 5. *An analytic signal is a complex-valued signal composed of a real-valued signal and its Hilbert transform. Taking $h_j(t)$ as an example, its analytic signal, $h_i{}^z(t)$, can be expressed in the form expressed in (15).*

$$h_i^z(t) = h_i(t) + j\mathcal{H}[h_i(t)] = A_i(t)e^{j2\pi*\Psi_i(t)} \tag{15}$$

By applying the Hilbert transform to extend hi(t) into $h_i{}^z$(t) and rewriting it into the form on the right-hand side of the second equality in (15), the instantaneous frequency and instantaneous amplitude of component $h_i(t)$ can be obtained, enabling the extraction of its time–frequency trajectory and instantaneous amplitude features.

Considering the multi-component coupling characteristics of power signals, the proposed adaptive time-varying signal model represents the power signal as the superposition of multiple $h_i(t)$ signal components. Moreover, coupling terms of the form $h_i(t) \times h_j(t)$ can be equivalently transformed into a sum of trigonometric components via product-to-sum identities and thus can still be represented within the proposed multi-component framework. Due to the widespread presence of dc-link components, a polynomial trend, $P(t)$, is introduced to replace the constant term a_0 in the classical harmonic model.

Based on this analysis of power equipment operating characteristics, three fundamental types of non-stationary features in power signals can be summarized, and a corresponding quasi-periodic harmonic signal model can be established. Using this model, complex time-varying characteristics commonly observed in non-stationary power signals can be effectively characterized, including random time-varying frequency shifts, high-frequency transient amplitude variations, multi-scale coupling, and multiple oscillatory behaviors derived from the three fundamental non-stationary features.

$$G(t) = F(t) + P(t) + \varepsilon(t) \tag{16}$$

In this paper, the constant term coefficient a0 in (11) is replaced by $P(t)$; the harmonic coefficients $a_1, a_2, \ldots, a_K$ are replaced by the time-varying functions $A_1(t), A_2(t), \ldots, A_K(t)$;

the original frequency components are replaced by the integrals of integrable functions $f(s)$; and $\varepsilon(t)$ denotes the noise term.

$$\begin{cases} F(t) = \sum_{i=1}^{K} h_i(t) \\ h_i(t) = A_i(t)\cos\left(2\pi * \int_0^t f_i(s)ds\right) \end{cases} \tag{17}$$

where the function $f_j(t)$ represents the instantaneous frequency of component $h_i(t)$ at time t, and $A_j(t)$ denotes the instantaneous amplitude of component $h_i(t)$ at time t.

2.3. Feature Extraction and Reconstruction Method for Non-Stationary Signals

2.3.1. Overview of the Proposed Method

According to the adaptive non-stationary signal model proposed in Section 3, the signal, $G(t)$, is first preprocessed to extract the trend component, $P(t)$, so that subsequent analysis can focus on complex non-stationary features. Meanwhile, to accurately analyze the wide dynamic range, fast time-varying behavior, and strong randomness of the signal, the adopted preprocessing method should not introduce any shift in the original time–frequency trajectories or amplitude characteristics of $F(t)$, as detailed in Ref. [27].

To achieve an accurate analysis of the non-stationary features in $F(t)$, the proposed method mainly consists of two steps.

(1) An improved scaling-basis chirplet transform is applied to $F(t)$ to obtain a time–frequency representation with enhanced resolution, enabling intuitive and precise characterization of signal variations.

(2) An improved ridge detection algorithm is employed to extract the corresponding time–frequency trajectories and instantaneous amplitude features from the time–frequency distribution.

To controllably reconstruct the given target non-stationary features, this paper proposes a power signal reconstruction method based on cross-correntropy. By constructing a unified reconstruction parameter framework, the proposed method enables accurate recovery of the target non-stationary features while ensuring the consistency of signal characteristics before and after reconstruction. The overall framework of the proposed method is illustrated in Figure 5.

2.3.2. Improved Scaling-Basis Chirplet-Based Time–Frequency Representation Method

The conventional chirplet transform obtains the time–frequency representation of a signal by taking the inner product between the chirplet function and the input signal. The mathematical expression of the chirplet function is as follows:

$$g(t) = \frac{w_\sigma(t)}{\exp(j\frac{C}{2}t^2 + j\omega t)} \tag{18}$$

where t_0 denotes the time center; ω represents the center frequency; σ denotes the time support and controls the duration of the Gaussian window; and C represents the chirp rate, which determines the rate of frequency variation with time. The function $w_\sigma(t)$ is a non-negative, symmetric, and normalized real-valued window function, which is typically chosen as a Gaussian window:

$$w_\sigma(t) = \frac{1}{\sqrt{2\pi}\sigma}\exp(-\frac{t^2}{2\sigma^2}) \tag{19}$$

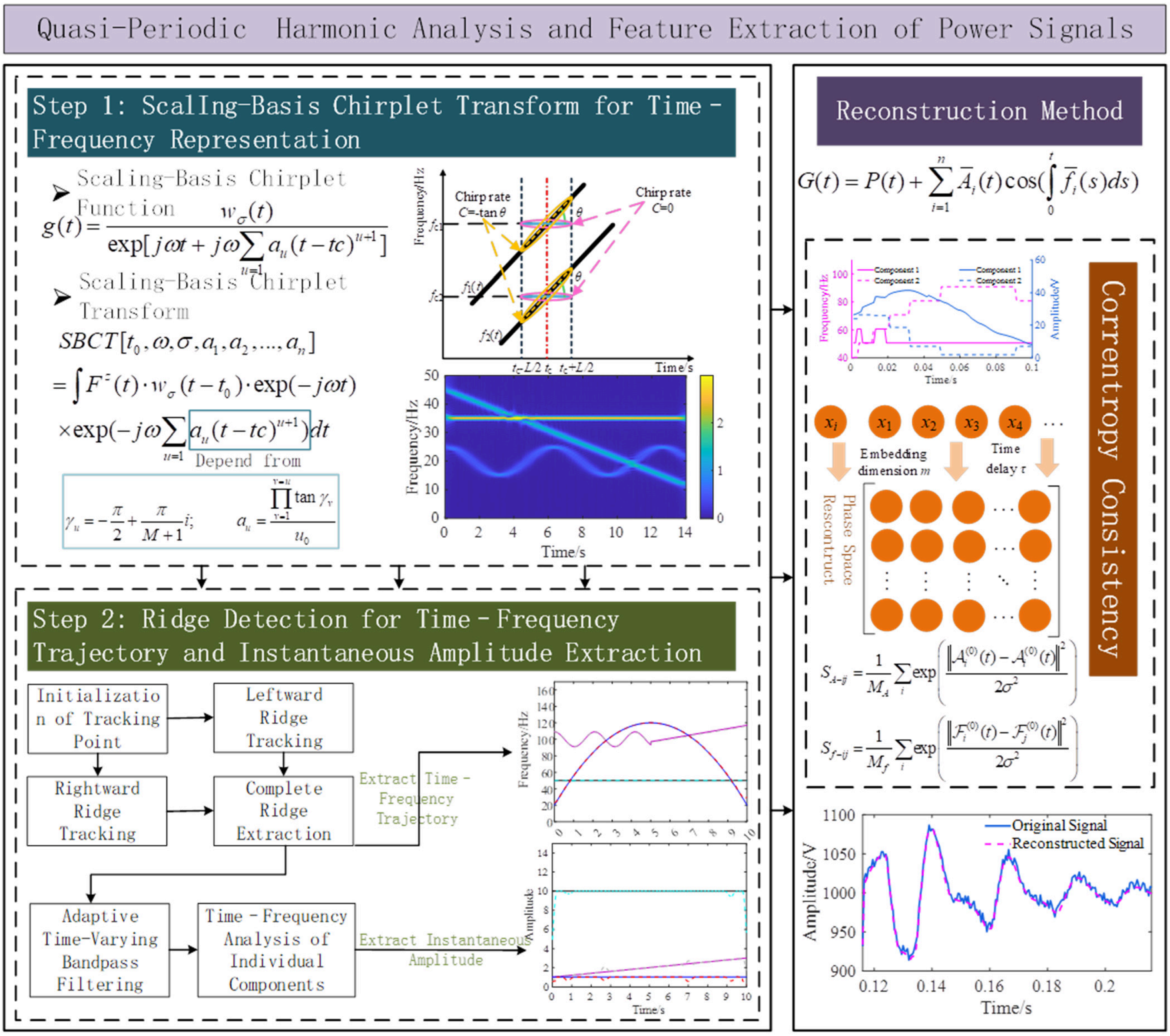

Figure 5. Framework of the proposed method.

Figure 6 illustrates the optimal matching principle between the chirplet parameters and the instantaneous frequency trajectory of a signal within a window of length L and time center t_c. The curves $f_1(t)$ and $f_2(t)$ represent two parallel time–frequency trajectories of signals, indicating that their chirp rates are constant over time and identical. To achieve an optimal time–frequency representation, the selected chirp-rate parameter must produce a rotation angle, θ, that matches the slope of the signal's instantaneous frequency trace [28,29]. The relationship between the chirp rate, C, and θ is expressed as $\theta = -\arctan(C)$.

When the conventional chirplet transform is applied to complex non-stationary power signals, three major challenges are encountered.

(1) The instantaneous frequency of power signals exhibits rapid variations on the millisecond scale, while the fixed chirp-rate parameter of the chirplet basis function is difficult to satisfy the optimal matching principle over the entire time domain and may even lead to energy dispersion.

(2) Power signals often contain multiple coexisting and coupled components. Therefore, a single-parameter family of the chirplet transform is unable to simultaneously satisfy

the optimal matching conditions for multiple components, which easily results in spectral overlap, cross-terms, and demixing deviations.

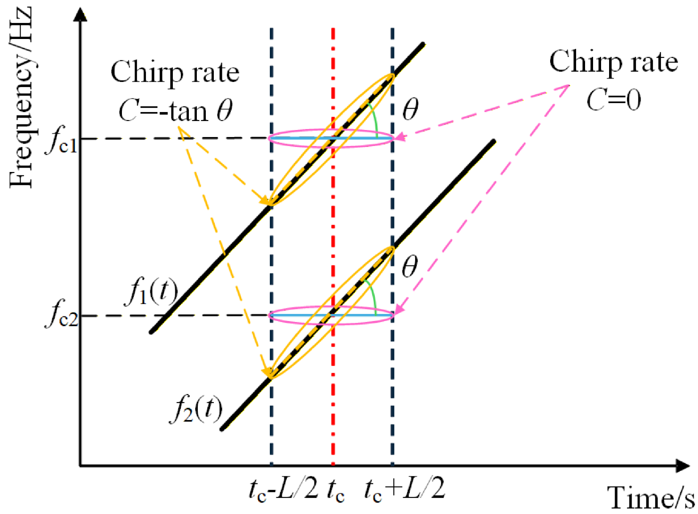

Figure 6. Chirplet parameter matching principle.

(3) The degree of non-stationarity in power signals varies across different time intervals, whereas the conventional chirplet transform performs time–frequency representation using a fixed window. In intervals where the chirp rate varies slowly, an excessively short window leads to insufficient effective samples and inaccurate time estimation, sacrificing time resolution. Conversely, in intervals with rapidly varying chirp rates, an overly long window causes significant non-stationarity and spectral broadening, resulting in degraded frequency resolution.

Although some improved methods have alleviated the first limitation of the conventional chirplet transform (CT) to a certain extent, the remaining critical issues have not been effectively resolved and continue to hinder efficient time–frequency energy concentration. This problem becomes particularly pronounced in multicomponent signal scenarios with closely spaced frequency components and strong noise interference.

To overcome these three limitations, a kernel function with a variable chirp rate is employed to dynamically adjust the slope and window scaling of the time–frequency basis function. Specifically, the chirp rate is defined as a function of the center frequency, the time center, and the integration variable [30]:

$$C = -\tan\theta = c(\omega, t_c, t) \tag{20}$$

Compared with the conventional CT, which employs a fixed chirp-rate formulation, Equation (18) introduces a multivariate dependency that enables the time–frequency basis function to adaptively vary with both time and frequency, achieving accurate matching of dynamically evolving instantaneous frequency trajectories.

To satisfy the requirements of flexible chirp-rate variation and adjustable time-window scaling, the transform basis function, $g(t)$, is constructed as follows:

$$g(t) = \frac{w_\sigma(t)}{\exp[j\omega(t - \sum\limits_{k=1}^{n} a_k(t - t_c)^{1+k})]} \tag{21}$$

where a_1, a_2, a_3, ..., a_n are parameters to be determined. The exponential term in the numerator is referred to as the phase function, which represents the rotation angle of $g(t)$ over the complex plane.

$$\varphi = \omega t + \omega \sum_{k=1}^{n} a_k (t - t_c)^{1+k} \tag{22}$$

The first-order and second-order derivatives of the phase function, φ, correspond to the instantaneous frequency, f, and the chirp rate, C, respectively:

$$f = \varphi' = \frac{d\varphi}{dt} \tag{23}$$

$$C = -\tan\theta = \frac{d\varphi'}{dt} \tag{24}$$

In summary, the time–frequency representation matrix obtained by the proposed improved scaling-basis Chirplet transform is as follows:

$$TFR(t_c, w) = \int_{-\infty}^{+\infty} F^z(t) w_\sigma(t - t_c) \exp[j\omega(t - \sum_{k=1}^{n} a_k (t - t_c)^{1+k})] dt \tag{25}$$

where TFR(t_c, ω) represents the intensity coefficient of the signal at frequency ω and time t_c, and $F^z(t)$ denotes the analytic signal of $F(t)$, which is obtained via the Hilbert transform operator; that is,

$$F^z(t) = F(t) + j\mathcal{H}[F(t)] \tag{26}$$

By visualizing the entire time–frequency distribution matrix, a time–frequency distribution map can be obtained, which enables intuitive characterization of the variation patterns of non-stationary features in power signals.

In terms of computational complexity, the main computational burden of the SBCT method arises from two aspects: (1) the generation of multiple sub-time–frequency representations (sub-TFRs) under different parameter combinations (γ_1, γ_2), and (2) the selection of optimal parameters at each time center based on the kurtosis criterion. Due to the need for exhaustive search over discretized angle spaces, the overall computational complexity can be expressed as $O(N_s MNL^2)$, where N_s denotes the signal length, L denotes the window size, and M and N represent the discretization levels of the chirp-related parameters. The computational cost increases significantly with larger window sizes and finer parameter discretization.

For real-time applications, such computational complexity may introduce latency, particularly for high-sampling-rate signals or long-duration data commonly encountered in power systems. However, in many of the practical scenarios in modern power systems—such as power quality assessment, harmonic analysis, and fault feature extraction—processing is typically performed in an offline or quasi-real-time manner, where strict real-time constraints are less critical. Therefore, the proposed method remains practically applicable in such contexts.

Moreover, the computational burden can be effectively alleviated through several strategies, including reducing the parameter discretization levels (i.e., decreasing M and N), adopting shorter analysis windows, and leveraging parallel computing techniques such as GPU acceleration. These approaches enable a favorable tradeoff between computational efficiency and time–frequency resolution, thereby facilitating the practical deployment of the SBCT method in power system applications.

2.3.3. Non-Stationary Feature Extraction Method

Although the scaling-basis chirplet transform can provide a high-resolution time–frequency distribution matrix (TFR), the components of power signals usually appear as finite-bandwidth energy bands, evolving over time in the time–frequency plane due to discrete sampling constraints. Therefore, further refinement of the time–frequency distribution is required in order to accurately quantify the time–frequency trajectories and instantaneous amplitudes at each time instant.

Ridge detection algorithms can automatically track ridges in the time–frequency distribution and enable the extraction of time–frequency trajectories and instantaneous amplitude features for single-component signals. However, when power signals contain multiple components with intersecting time–frequency trajectories, conventional ridge detection algorithms become ineffective. To address this issue, we propose an improved ridge detection algorithm to jointly extract time–frequency trajectories and instantaneous amplitude features for power signals with crossing components.

Definition 6. *Given a time–frequency representation,* TFR(t, ω)*, a ridge is defined as a curve formed by local maxima along the frequency axis.*

This improved ridge detection algorithm proceeds as follows. First, an initial point is selected as the starting point for ridge tracking. The ridge is then tracked point by point along the time axis in both the forward and backward directions to obtain the complete ridge. When $F(t)$ contains multiple components and the corresponding time–frequency representation includes multiple ridges, an adaptive time-varying bandpass filter is applied to demodulate $F(t)$ and separate the component associated with the extracted ridge from the overall time–frequency distribution.

In this algorithm, the initial point is chosen as the global maximum of the time–frequency representation, taking a time–frequency distribution, TFR(t, ω), containing K ridges as an example.

First, the peak point of a ridge in the time–frequency representation is identified:

$$(t_{\mathrm{m}}, \omega_{\mathrm{m}}) = \underset{t,\omega}{\mathrm{argmax}}\{\mathrm{TFR}(t, \omega)\} \tag{27}$$

where $\overline{f}(t_{\mathrm{m}}) = \omega_{\mathrm{m}}$, $\overline{\omega}_R = \omega_m$ and $\overline{\omega}_L = \omega_m$;

We traverse $r = m - 1, m - 2, \ldots, N$ and identify

$$\hat{\omega}_R = \underset{\omega \in [\overline{\omega}_L - \Delta\omega, \overline{\omega}_L + \Delta\omega]}{\mathrm{argmax}} \{\mathrm{TFR}(t_r, \omega)\} \tag{28}$$

where $\hat{f}(t_r) = \hat{\omega}_R$.

We traverse $p = m{-}1, m{-}2, \ldots, N$ and identify

$$\hat{\omega}_L = \underset{\omega \in [\overline{\omega}_L - \Delta\omega, \overline{\omega}_L + \Delta\omega]}{\mathrm{argmax}} \{\mathrm{TFR}(t_p, \omega)\} \tag{29}$$

where $\hat{f}(t_p) = \hat{\omega}_L$.

The final obtained $f(t)$ denotes the estimated ridge trajectory.

By tracking a ridge from its maximum point in the time–frequency map toward both the left and right directions, the time–frequency trajectory estimate of this ridge can be obtained. Subsequently, the signal, $F(t)$, is demodulated using an adaptive time-varying bandpass filter to extract the component associated with this ridge from $F(t)$. The cutoff frequencies of the time-varying bandpass filter for separating the j-th component are set as follows:

$$f_{\mathrm{j\_down}} = f_j(t) - \frac{1}{2}BW; \quad f_{\mathrm{j\_up}} = f_j(t) + \frac{1}{2}BW \tag{30}$$

where BW denotes the bandwidth for component discrimination, $f_{\mathrm{j\_down}}$ denotes the lower cutoff frequency, and $f_{\mathrm{j\_up}}$ denotes the upper cutoff frequency.

According to the Bedrosian theorem, the Hilbert transform is applied to each component of $F(t)$ to extract its instantaneous amplitude profile.

$$\hat{A}_j(t) = \left|F_j(t) + \mathcal{H}(F_j(t))\right| \tag{31}$$

where $\hat{A}_j(t)$ denotes the estimated instantaneous amplitude profile of the j-th component of $F(t)$.

By repeatedly applying (A1)–(A5), the time–frequency trajectories and instantaneous amplitude profiles of all K components can be obtained.

$$\bigcup_{j=1}^{K} \hat{f}_j(t) \approx \bigcup_{j=1}^{K} f_j(t) \tag{32}$$

$$\bigcup_{j=1}^{K} \hat{A}_j(t) \approx \bigcup_{j=1}^{K} A_j(t) \tag{33}$$

2.3.4. Cross-Correntropy-Based Non-Stationary Signal Reconstruction Method

To ensure that the proposed reconstruction method expands the feature library of power signals without compromising the consistency of signal characteristics before and after reconstruction, a signal reconstruction method based on cross-correntropy is proposed, in which inter-component constraints are imposed to achieve this objective.

According to analytic signal theory, when the original signal satisfies the strictly asymptotic monocomponent condition, reconstructing the signal components based on $f_i(t)$ and $A_i(t)$ allows the signal characteristics to be recovered without distortion. This property enables the extraction and analysis of non-stationary features using time–frequency trajectories and instantaneous amplitudes, providing a mathematical foundation for non-stationary power metering, feature library construction for fault identification, and the reproduction of complex arc scenarios.

From an information-theoretic perspective, the time–frequency trajectory and instantaneous amplitude already contain all the information of the original signal. Based on the time–frequency trajectory and instantaneous amplitude profile, signal reconstruction should follow the following unified parameterization framework:

$$G(t) = \Re\left\{[A_{\mathrm{rec}}(t)]^T \odot e^{j\Psi_{\mathrm{rec}}(t)}\right\} + P(t) \tag{34}$$

where $\Re\{\}$ denotes the real-part operator; $P(t)$ represents the polynomial trend obtained by the aforementioned polynomial extraction operator; and the instantaneous amplitudes and time–frequency trajectories of the reconstructed components are denoted by the vector-valued functions $A_{\mathrm{rec}}(t)$ and $\Psi_{\mathrm{rec}}(t)$, respectively.

$$A_{\mathrm{rec}}(t) = \begin{bmatrix} A_{1\_\mathrm{rec}}(t) \\ A_{2\_\mathrm{rec}}(t) \\ \vdots \\ A_{K\_\mathrm{rec}}(t) \end{bmatrix} \tag{35}$$

$$\Psi_{\text{rec}}(t) = \begin{bmatrix} \int_0^t f_{i\_\text{rec}}(s)ds \\ \int_0^t f_{2\_\text{rec}}(s)ds \\ \vdots \\ \int_0^t f_{K\_\text{rec}}(s)ds \end{bmatrix} \quad (36)$$

The signal reconstruction method proposed in this paper for expanding the feature library of power signals essentially aims to infer the observations of power signals under other system states based on the observed power signal, $F(t)$, under a local operating state, in the presence of unknown parameters in the complex high-dimensional state-space equations of power systems. The analysis proceeds as follows: it is assumed that the power system evolves on a d-dimensional manifold, $\mathcal{M}$.

$$\dot{x} = g(x), x \in \mathcal{M} \quad (37)$$

The time–frequency trajectory and instantaneous amplitude of the i-th observed component of the power signal are expressed as

$$f_{i\_\text{mea}}(t) = H_1(x(t)) + v_1, H_1 : \mathcal{M} \to \mathbb{R} \quad (38)$$

$$A_{i\_\text{mea}}(t) = H_2(x(t)) + v_2, H_2 : \mathcal{M} \to \mathbb{R} \quad (39)$$

where v_1 and v_2 are measurement error vectors.

The delay-embedded vectors obtained from f_{i_mea} and A_{i_mea} through phase-space reconstruction are expressed as

$$\mathcal{F}_i^{(0)}(t) = \begin{bmatrix} f_{i\_\text{mea}}(t) \\ f_{i\_\text{mea}}(t-\tau) \\ \vdots \\ f_{i\_\text{mea}}(t-(m-1)\tau) \end{bmatrix} \quad (40)$$

$$\mathcal{A}_i^{(0)}(t) = \begin{bmatrix} A_{i\_\text{mea}}(t) \\ A_{i\_\text{mea}}(t-\tau) \\ \vdots \\ A_{i\_\text{mea}}(t-(m-1)\tau) \end{bmatrix} \quad (41)$$

where m denotes the embedding dimension, and τ represents the time delay.

According to Takens' embedding theorem, when the embedding dimension satisfies $m \geq 2d + 1$, the trajectory of the delay vectors in the reconstructed phase space is homeomorphic to that of the original system in the state space. Due to the inherently complex, large-scale, and strongly coupled nature of power systems, the underlying dynamical process is generally characterized by a high-dimensional state space. The theoretical attractor dimension, d, associated with such systems is typically much higher than the effective dimensionality required for practical signal reconstruction.

In this article, the delay embedding employed is not intended to recover the full dynamical manifold of the original system but rather to construct a reduced-order representation that preserves the dominant temporal dependencies and inter-component structures of the observed signals. Therefore, an embedding dimension, $m = 10$, is adopted. This value is selected in a conservative sense to satisfy the Takens condition, $m \geq 2d + 1$, while balancing reconstruction capability and computational efficiency. As a result, the validity of phase space reconstruction is ensured without introducing unnecessary dimensional expansion.

Consequently, the cross-correntropy between the delay-embedded vectors of the different components of the original signal can be used to impose constraints on the relationships among the reconstructed components. These constraints are represented by the matrices S_A and S_f:

$$S_A = \begin{bmatrix} S_{A-11} & S_{A-12} & \cdots & S_{A-1K} \\ S_{A-21} & S_{A-22} & \cdots & S_{A-2K} \\ \vdots & \vdots & \ddots & \vdots \\ S_{A-K1} & S_{A-K2} & \cdots & S_{A-KK} \end{bmatrix} \tag{42}$$

$$S_f = \begin{bmatrix} S_{f-11} & S_{f-12} & \cdots & S_{f-1K} \\ S_{f-21} & S_{f-22} & \cdots & S_{f-2K} \\ \vdots & \vdots & \ddots & \vdots \\ S_{f-K1} & S_{f-K2} & \cdots & S_{f-KK} \end{bmatrix} \tag{43}$$

where S_{A_ij} denotes the cross-correntropy between the delay-embedded vectors of the instantaneous amplitudes of components i and j, and S_{f_ij} denotes the cross-correntropy between the delay-embedded vectors of the time–frequency trajectories of components i and j. The corresponding calculation methods are as follows:

$$S_{A-ij} = \frac{1}{M_A} \sum_i \exp\left(\frac{\left\| \mathcal{A}_i^{(0)}(t) - \mathcal{A}_i^{(0)}(t) \right\|^2}{2\sigma^2} \right) \tag{44}$$

$$S_{f-ij} = \frac{1}{M_f} \sum_i \exp\left(\frac{\left\| \mathcal{F}_i^{(0)}(t) - \mathcal{F}_j^{(0)}(t) \right\|^2}{2\sigma^2} \right) \tag{45}$$

where M_A denotes the dimensionality of the vectors $\mathcal{A}_i$ and $\mathcal{A}_j$, M_f denotes the dimensionality of the vectors $\mathcal{F}_i$ and $\mathcal{F}_j$, and σ represents the window width of the Gaussian kernel function.

Given that both S_A and S_f are symmetric positive definite matrices, a linear mixing matrix, V, can be applied to the original component vectors, A_{mea} and Ψ_{mea}, during reconstruction to obtain the time–frequency trajectory vector and the instantaneous amplitude vector of the reconstructed signal:

$$A_{\text{rec}}(t) = V_A A_{mea}(t) \tag{46}$$

$$f_{\text{rec}}(t) = V_f f_{\text{mea}}(t) \tag{47}$$

When V satisfies the following conditions, the cross-correntropy between the delay-embedded vectors of each component remains unchanged before and after reconstruction, preserving the inter-component relationships:

$$S_A = V S_A V^T \tag{48}$$

$$S_f = V S_f V^T \tag{49}$$

By applying the reconstructed time–frequency trajectories and instantaneous amplitudes $A_{\text{rec}}(t)$ and $f_{\text{rec}}(t)$ to the reconstruction framework described in (46) or (47), a series of signals, $G_{\text{rec}}(t)$, can be obtained to expand the signal feature library. Since the transformation matrices, V_A and V_f, that satisfy (48) or (49) are not unique, the reconstructed signals are also not unique.

3. Results

3.1. Numerical Signal Experiments

To evaluate the proposed time–frequency method under conditions where the ground truth is known, a representative numerical signal containing non-stationary characteristics of power signals is synthetically constructed. The sampling frequency is set to f_s = 20 kHz, and the signal duration is 1 s. The fundamental frequency is 50 Hz, and the fundamental amplitude is taken as the reference value and normalized to 1 p.u. In addition, typical third-, fifth-, and seventh-order harmonics are superimposed, with normalized amplitudes of 0.12, 0.07, and 0.05 p.u., respectively, to characterize common low-order harmonic components.

To reflect quasi-periodic harmonic components commonly encountered in practical engineering scenarios, two non-stationary feature components are further introduced as follows:

(1) A narrowband non-stationary component is introduced over the interval $t \in [0.20, 0.60]$ s to represent frequency migration phenomena formed on the AC side after DC-side power fluctuations are processed through power-electronic conversion. Its time–frequency trajectory is constructed as the superposition of a trend term, a bounded chirp term, and a low-frequency jitter term:

$$\begin{gathered} f_1(t) = f_{\text{ref}}(\tau) + \Delta f_{\text{mod}}(\tau) + \delta f_{\text{jit}}(\tau) \\ \tau = t - t_1 \in [0, 0.40] \end{gathered} \tag{50}$$

where t_1 = 0.20 s. The trend term $f_{\text{ref}}(\tau)$ originates from DC-side power disturbances and is constructed from five characteristic frequency points, (τ_i, f_i), i = 0, . . ., 4, specifically, (τ_0, f_0) = (0, 75), (τ_1, f_1) = (0.10, 130), (τ_2, f_2) = (0.22, 25), (τ_3, f_3) = (0.32, 100), and (τ_4, f_4) = (0.40, 70), which are interpolated using the Newton interpolation method.

$$f_{ref}(\tau) = \sum_{i=0}^{4} f_i \updownarrow_i, \updownarrow_i = \prod_{j=0, j \neq i}^{4} \frac{\tau - \tau_j}{\tau_i - \tau_0} \tag{51}$$

The bounded chirp term, $\Delta f_{\text{mod}}(\tau)$, approximately represents fluctuations induced by complex control structures, such as current loops and voltage loops. It is generated through the following bounded, zero-mean chirp modulation strategy.

$$\Delta f_{\text{mod}}(\tau) = M(\tau) \sum_{i=1}^{K} \kappa_k \sin(2\pi \nu_i \tau + \xi_k) \tag{52}$$

$$M(\tau) = M_0 + M_1 \sin(2\pi \nu_{\text{e}} \tau + \xi_{\text{e}}) \tag{53}$$

where M_0 = 0.6, M_1 = 0.4, v_{e} = 0.5, $\xi_1 = \xi_2 = \xi_3 = \xi_{\text{e}} = 0$, κ_1 = 6, κ_2 = 2.5, and κ_3 = 1.2.

The random jitter term originates from unmodeled perturbations and is generated according to the following strategy:

$$\delta f_{\text{jit}}(\tau) = (h_{2\text{HZ}} * w)(\tau) \tag{54}$$

where $h_{2\text{Hz}}$ denotes the impulse response of a second-order low-pass filter, $*$ denotes the convolution operator, and $w(\tau)$ represents white noise.

To reflect high-frequency transient amplitude variation characteristics, the amplitude envelope of the first non-stationary component is generated according to the following strategy:

$$\begin{aligned} A_1(t) &= A_0 w_{\mathrm{H}}(\tau) \exp[\sigma_a (h_{\mathrm{b}} * w)(\tau)] \\ \tau &= t - t_1 \in [0, 0.40] \end{aligned} \tag{55}$$

where $w_{\mathrm{H}}(\tau)$ denotes a Hanning start–stop window, σ_a is set to 0.2, h_{b} represents a second-order Butterworth filter, $w(\tau)$ denotes white noise, and $*$ indicates the convolution operator.

(2) A frequency-shift component centered around 350Hz is introduced over the interval $t \in [0.75, 0.95]$ s, corresponding to continuous spectral components that may arise in a six-pulse rectifier operating under stochastic modulation strategies. The amplitude of this component is set to 0.2 p.u., and the frequency drift effect is approximated by $\delta f(\tau)$:

$$\begin{aligned} f_2(t) &= 7 f_g + \delta f(\tau) \\ \tau &= t - t_2 \in [0.75, 0.95] \end{aligned} \tag{56}$$

where f_{g} = 50 Hz and t_2 = 0.75 s.

The time-domain waveform of the synthesized numerical signal is shown in Figure 7, in which the two non-stationary features are present over the time intervals 0.2–0.6 s and 0.75–0.95 s, respectively.

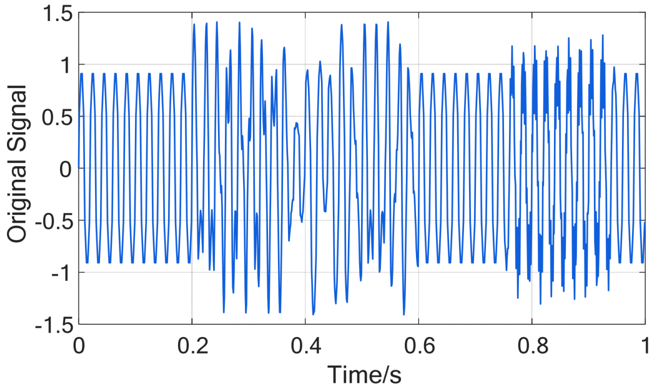

Figure 7. Time-domain waveform of the synthesized numerical signal.

The time–frequency distributions of the signal $x(t)$ were obtained using six methods—STFT, CWT, WVD, GLCT, VSLCT, and the proposed improved SBCT—and are compared with the ideal time–frequency distribution, as illustrated in Figure 8. The two regions containing non-stationary features are highlighted by red solid boxes.

The identification performance of the six methods for the fundamental component, three harmonic components, and two non-stationary components is summarized in Table 1. In addition, Rényi entropy is adopted as a quantitative metric to evaluate the time–frequency concentration capabilities, with the corresponding results presented in Table 2. A lower Rényi entropy value indicates a higher degree of energy concentration in the time–frequency representation (TFR) and thus reflects the corresponding method's stronger ability to characterize variations in non-stationary features [31].

The comparative results indicate that different time–frequency analysis methods exhibit clear performance differences and application preferences when dealing with multi-component non-stationary signals.

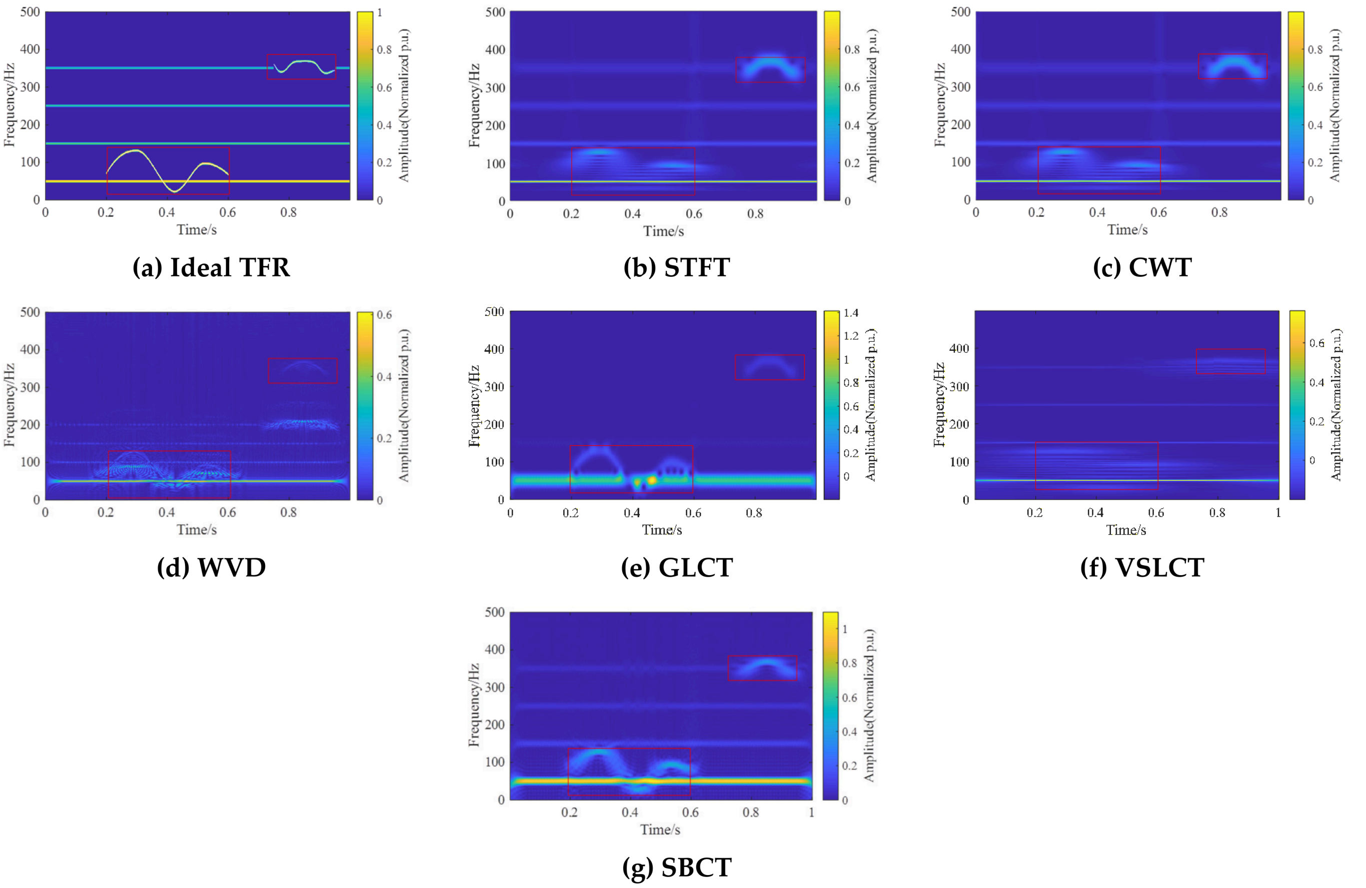

Figure 8. Comparison of processing results obtained using different time–frequency methods.

Table 1. Energy intensity of each signal component obtained using different time–frequency analysis methods.

Methods	STFT	CWT	WVD	GLCT	VSLCT	SBCT
Fundamental Component	85.0169%	92.8605%	84.1928%	89.1236%	94.3962%	97.9195%
3rd Harmonic Component	81.9669%	88.6922%	49.1330%	42.4731%	93.1768%	85.3279%
5th Harmonic Component	77.5822%	86.7997%	16.1518%	20.2574%	87.1470%	83.8016%
7th Harmonic Component	66.1888%	79.0270%	12.2956%	17.6778%	84.5655%	81.4941%
Non-Stationary Component 1	62.7674%	69.8723%	58.8927%	86.6582%	47.3238%	93.2906%
Non-Stationary Component 2	85.5046%	87.7354%	73.5745%	88.5033%	38.8904%	81.1252%

Table 2. Rényi entropy values corresponding to the four methods.

Methods	STFT	CWT	WVD	GLCT	VSLCT	SBCT
Rényi Entropy	19.13	12.12	11.90	13.45	10.67	9.81

For conventional methods, both STFT and CWT rely on fixed basis functions, which limit their time–frequency resolution. This results in evident energy diffusion in non-stationary regions. For example, in non-stationary component 1, the identification accuracies of STFT and CWT are only 62.77% and 69.87%, respectively, making it difficult to accurately capture complex frequency variations. Although WVD provides high theoretical time–frequency resolution, it is sensitive to cross-term interference in multi-component signals. This leads to spurious components around 100 Hz and 200 Hz that do not exist in the original signal. These false components distort the energy distribution in nearby regions and reduce the accuracy of representing true signal components. For non-stationary component 2, where cross-term interference is weaker, WVD achieves an accuracy of 73.57%. However, near non-stationary component 1, dense cross-terms severely mask the true structure, and the accuracy drops to 58.89%.

For improved chirplet-based methods, GLCT and VSLCT show complementary strengths but also clear limitations. GLCT performs well in representing non-stationary components, with accuracies of 86.66% and 88.50% for components 1 and 2, respectively. However, its performance on harmonic components is poor. The identification accuracies for the third, fifth, and seventh harmonics are only 42.47%, 20.26%, and 17.68%, respectively, which are about 50% lower than those of SBCT. This is because its chirp-rate matching mechanism is more suitable for non-stationary components than for stationary harmonics.

By contrast, VSLCT performs well in harmonic identification. The accuracies for the third, fifth, and seventh harmonics reach 93.18%, 87.15%, and 84.57%, respectively, outperforming both GLCT and traditional methods. However, its performance on non-stationary components is significantly worse. The accuracies for components 1 and 2 are only 47.32% and 38.89%, which are about 46% and 42% lower than those of SBCT. This is mainly because VSLCT assumes proportional frequency relationships among components, which is suitable for harmonics but not for asynchronous and nonlinear frequency variations.

In comparison, the proposed SBCT achieves consistently strong performance across all components. For harmonic components, the accuracies for the third, fifth, and seventh harmonics are 85.33%, 83.80%, and 81.49%, respectively, which are significantly higher than those of GLCT and close to VSLCT. For non-stationary components, SBCT achieves 93.29% and 81.13%, outperforming VSLCT and matching or exceeding GLCT. This demonstrates that SBCT can effectively handle both harmonic and non-stationary components.

In addition, from the perspective of energy concentration, SBCT has the lowest Rényi entropy value (9.81). Compared with STFT (19.13), it is reduced by about 48.7%, and compared with GLCT (13.45), it is reduced by about 27.1%. This indicates that SBCT provides better time–frequency energy concentration.

3.2. Simulation Signal Experiments

To objectively evaluate the performance of the proposed method in analyzing power signals containing quasi-periodic harmonic components, a three-phase isolated two-level DC/DC charging station simulation model, as shown in Figure 9, is constructed. This model is used to simulate non-stationary feature signals generated by the converter under different representative operating conditions.

The mean square error (MSE), denoted as e_{mse}, is used as the evaluation metric and is defined as follows:

$$e_{mse} = \sqrt{(1/n)\sum_{i=1}^{n}\left|\left|G(i) - \hat{G}(i)\right|\right|_2^2} \tag{57}$$

where $G(i)$ denotes the original signal, and $\hat{G}(i)$ represents the reconstructed signal obtained from the estimated time–frequency trajectories and instantaneous amplitudes.

To investigate the feature extraction capability of different methods under varying noise levels, multiple signal-to-noise ratio (SNR) scenarios are considered to compare the performance of ridge detection algorithms combined with the four time–frequency representation methods in extracting non-stationary features. The SNR is defined based on signal energy as follows.

$$\mathrm{SNR} = 10\log_{10}\left(\frac{\sum_t G^2(t)}{\sum_t n^2(t)}\right) \tag{58}$$

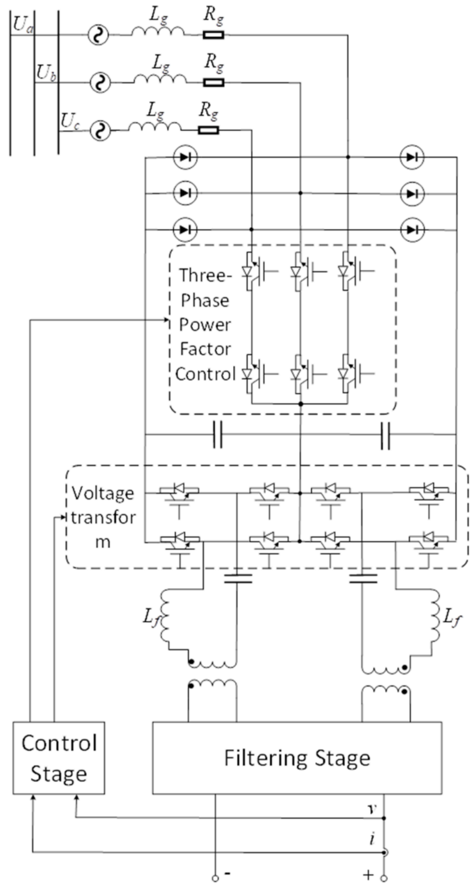

Figure 9. Simulation model of a DC charging station.

For comparison, five time–frequency analysis methods—STFT, CWT, WVD, GLCT, and VSLCT—are selected as benchmark approaches. To improve the statistical reliability of the results, 50 independent trials are conducted under each signal-to-noise ratio (SNR) condition. The mean values and confidence intervals are then calculated to reduce the influence of random noise. The performance of each method is visualized using error bars, which reflect their overall behavior and stability under different noise levels. The corresponding results are shown in Figure 10.

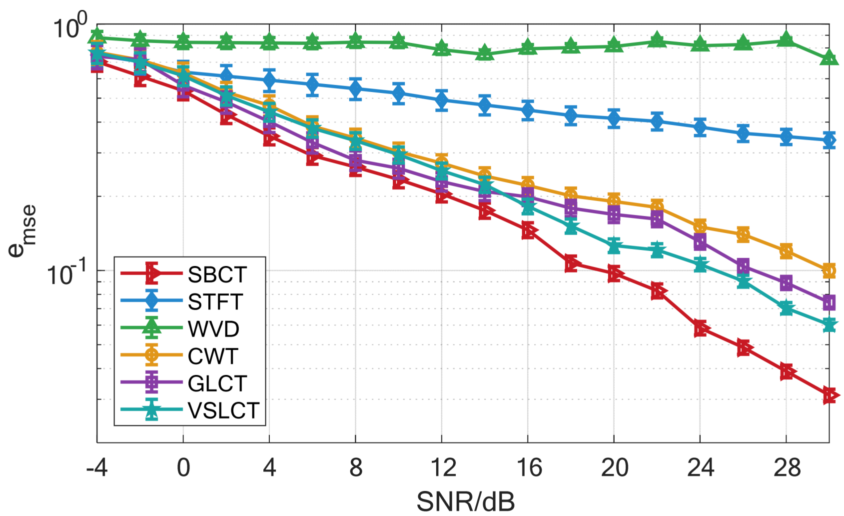

Figure 10. Feature extraction errors of different time–frequency methods.

As shown in Figure 10, the mean square error (MSE) of all methods decreases as the signal-to-noise ratio (SNR) increases. However, the performance differences among methods become more evident. SBCT consistently achieves the lowest error across the entire SNR range and shows a faster convergence rate. For example, under medium-to-high SNR conditions (SNR $\geq$ 10 dB), the error of SBCT is reduced by about 52–91% compared with STFT; 22–48% compared with GLCT; and 32–69% and 22–38% compared with CWT and VSLCT, respectively. This demonstrates a clear accuracy advantage.

Under low SNR conditions (SNR $\leq$ 0 dB), the errors of different methods are relatively close. However, WVD maintains a higher error due to cross-term interference. For instance, at SNR = 0 dB, the error of WVD is about 0.842, while that of SBCT is about 0.537, which is approximately 57% lower. As the SNR increases, the advantage of SBCT becomes more pronounced. By contrast, STFT and GLCT show slower error reduction, indicating certain performance limitations. Although VSLCT and CWT improve with increasing SNR, their errors remain noticeably higher than those of SBCT.

In the high SNR region (SNR $\geq$ 20 dB), all methods gradually approach convergence. The error of SBCT decreases from about 0.097 at 20 dB to about 0.031 at 30 dB. In comparison, STFT and GLCT remain within the ranges of about 0.41–0.34 and 0.17–0.06, respectively. SBCT continues to show a decreasing trend, indicating a stronger ability to utilize high-SNR information.

In addition, the error bars indicate that SBCT has smaller confidence intervals under all noise conditions. For example, when SNR $\geq$ 10 dB, the confidence interval of SBCT is about 0.015–0.002, while that of STFT is about 0.049–0.023, and that of GLCT is about 0.023–0.003. This means that the fluctuation range of SBCT is reduced by about 40–70% compared with STFT and 20–50% compared with GLCT, showing better stability and statistical robustness.

3.3. Experimental Results on Measured Signals

In this subsection, the voltage waveform measured during the pre-charging stage of a 700 V high-power public DC fast charging station is analyzed and reconstructed. The rapidly varying DC voltage waveform during charging is shown in Figure 11. The polynomial trend is first extracted from this waveform, yielding the trend component shown in Figure 12a and the non-stationary component shown in Figure 12b.

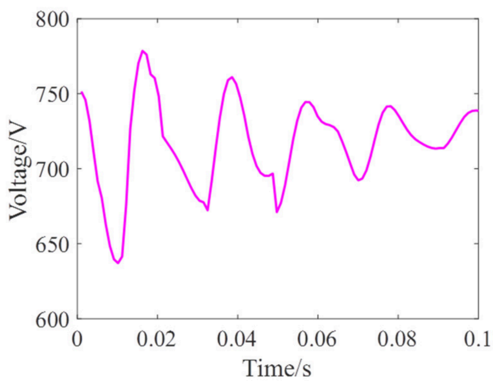

Figure 11. DC voltage waveform.

The time–frequency distribution of the non-stationary component shown in Figure 12b is presented in Figure 12. The signal energy is mainly concentrated in the low-frequency range (approximately 20–100 Hz) and within 0–0.04 s, which is consistent with the instantaneous amplitude peaks of the two components occurring before 0.04 s and their time–frequency trajectories being located below 100 Hz. For clarity, the black and red solid lines in the figure denote the corresponding ridges of the signal shown in Figure 12b.

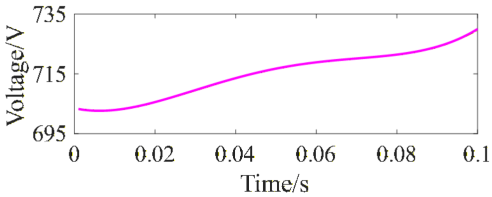

(a) Polynomial trend term

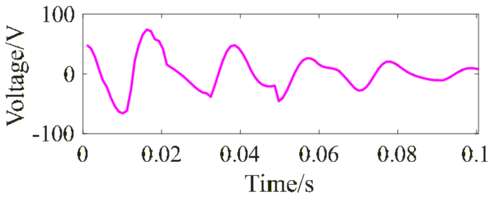

(b) Non-stationary component

Figure 12. Polynomial trend removal.

Using the ridge detection algorithm described in Section 2.3.3, the time–frequency trajectories and corresponding instantaneous amplitude features of two representative components are extracted from Figure 13, with the results shown in Figure 14. Component 1 exhibits frequency drift around 50 Hz, with its amplitude increasing and then decreasing, reaching a peak at approximately 0.03 s, which can be attributed to residual coupling and tracking errors in the outer loop of the PLL. Component 2 appears as a step-like low-frequency cluster associated with operating condition transitions of the charging station and the battery equivalent circuit, and its amplitude attenuates during the switching instant.

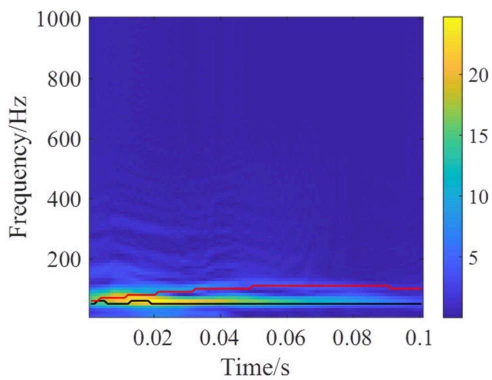

Figure 13. Time–frequency representation of the signal shown in Figure 12b.

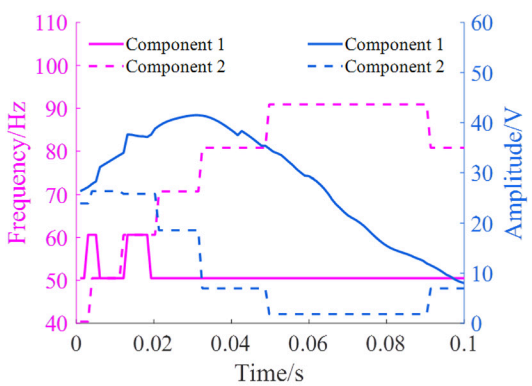

Figure 14. Results of ridge detection applied to Figure 13.

In Figure 15, the pink solid line represents a field-measured waveform from a 1000 V DC charging station, which is reconstructed using the method described in Section 2.3.4. The dashed line in the enlarged view of Figure 14 shows that the reconstructed waveform exhibits a high degree of consistency with the original waveform in both the overall trend and local disturbance characteristics. Quantitatively, the mean square error (MSE) between the reconstructed and original signals is 0.2324%, indicating that the proposed method achieves accurate reconstruction while effectively preserving the essential features of the original signal.

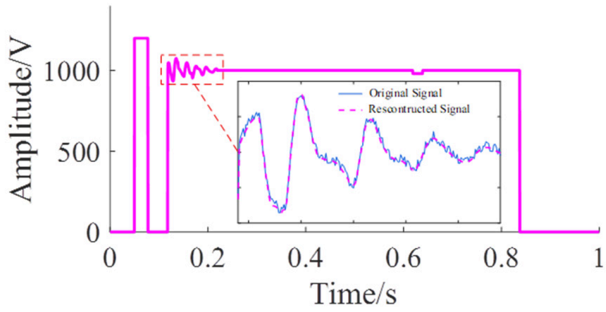

Figure 15. Comparison of measured and reconstructed waveforms of a 1000 V DC charging pile.

The reconstruction consistency confirms the effectiveness of the proposed method for measured power system signals and its ability to support accurate identification of complex non-stationary features under the "dual-high and dual-random" scenario.

3.4. Reconstruction Method Comparison Experiment

3.4.1. Dataset Description

To validate the effectiveness of the proposed power signal reconstruction method, experiments are conducted using a public synchronous motor electrical fault dataset from Sun et al. The dataset is built on a real experimental platform and includes six classes: five fault types and one normal condition [32]. The fault types are opened phase (OP), two-phase short circuit (2PSC), single-phase-to-ground fault (1PSC), rotor excitation voltage disconnection (REVD), and variation of rotor excitation current (VREC), along with the normal condition (NF). The specific details are shown in Table 3.

Table 3. Number of samples and fault labels.

Fault Type	Number	Label	Percent/%
NF	3259	0	61.01%
OP	703	1	13.16%
2PSC	518	2	9.69%
1PSC	753	3	14.09%
REVD	76	4	1.42%
VREC	32	5	0.59%

Each fault is collected through multiple independent experiments, each lasting about 1 s, with random fault occurrence times. Each sample is a multi-channel time series, including three-phase stator voltages (V_a, V_b, and V_c); three-phase stator currents (I_a, I_b, and I_c); rotor current, Ir; and rotational speed, ω, providing eight measurement channels. The data are segmented using fixed-length windows with a sampling interval of 1 ms.

3.4.2. Reconstruction Method Comparison

To validate the effectiveness of the proposed signal reconstruction method, several commonly used data augmentation methods are selected for comparison, including Random Oversampling (ROS), SMOTE, and Generative Adversarial Networks (GANs).

To evaluate the similarity between the generated samples and the original training samples, each method is used to augment the minority fault classes until their sizes match that of the normal class. Furthermore, the Fréchet Inception Distance (FID) and symmetric Mean Absolute Percentage Error (sMAPE) are adopted as evaluation metrics to quantitatively assess the quality of the generated samples. The calculation of FID is provided in Equation (59).

$$FID(p_r, p_g) = \|\mu_r - \mu_g\|_2^2 + tr\left(Cov_r + Cov_g - 2\sqrt{Cov_r Cov_g}\right) \tag{59}$$

where μ_r and μ_g denote the means of the original samples and reconstructed samples, respectively. Cov_r and Cov_g represent their covariance matrices, and tr denotes the trace of a matrix.

The calculation of sMAPE is provided in Equation (60).

$$sMAPE = \frac{1}{n}\sum_{i=1}^{n}\left(\frac{|\hat{x}_i - x_i|}{(\hat{x}_i + x_i)/2}\right) \times 100\% \tag{60}$$

where n denotes the number of samples, $\hat{x}_i$ represents the reconstructed value, and x_i denotes the true value.

The experimental results are shown in Table 4.

Table 4. Processing results for different methods.

Methods	FID	sMAPE
ROS	3.53	44.95
SMOTE	2.21	18.98
GAN	0.85	12.79
The Proposed Reconstruction Method	0.52	7.96

ROS performs the worst on both metrics. Its FID reaches 3.53, and its sMAPE is 44.95%, indicating that simple duplication fails to capture the true data distribution and leads to large numerical deviations. The SMOTE method generates new samples through interpolation, which improves distribution consistency and reduces error to some extent. However, its FID and sMAPE are still 2.21 and 18.98%, respectively, showing noticeable deviations. In comparison, GAN can learn the underlying data distribution. Its FID decreases to 0.85 and its sMAPE to 12.79%, demonstrating better generation capability. The proposed method achieves the best results on both metrics, with an FID of only 0.52 and an sMAPE of 7.96%. This indicates that the generated samples are closer to the real samples in both global distribution and local numerical characteristics.

3.4.3. Generalization Performance Evaluation

To verify the generalization ability of the proposed reconstruction method, multiple imbalanced datasets are constructed based on the original dataset. Specifically, the number of samples in the majority class (NF) is kept unchanged, while the samples of minority classes are randomly reduced to form different imbalance ratios.

Three representative classification models, namely SVM, LSTM, and CNN, are selected to validate the effectiveness of the proposed reconstruction method. By constructing datasets with varying degrees of imbalance, the robustness of the model under different data distributions can be systematically evaluated. Several imbalance ratios are considered, as shown in Table 5, where the ratio is defined as the proportion of sample numbers across the six classes. The reconstruction process balances the number of minority fault samples to be equal to that of other fault classes. The comparison results of classification accuracies obtained by different models on the original datasets and the reconstructed datasets under five cases are shown in Table 6.

Table 5. Imbalanced dataset configuration.

Case	Minor Fault Classes with Small Sample Sizes	Data Ratio (0:1:2:3:4:5)
Case 1	Fault 4,5	3259:703:518:753:76:32
Case 2	Fault 1,4,5	3259:70:518:753:76:32
Case 3	Fault 2,4,5	3259:703:51:753:76:32
Case 4	Fault 3,4,5	3259:703:518:75:76:32
Case 5	Fault 1,2,3,4,5	3259:70:51:75:76:32

Table 6. Model identification performance before and after reconstruction-based augmentation.

Case	SVM Accuracy	LSTM Accuracy	CNN Accuracy
Case 1	92.14%	94.42%	97.30%
Case 1(reconstructed)	92.47%	95.13%	97.86%
Case 2	92.98%	93.15%	97.93%
Case 2(reconstructed)	93.81%	94.12%	98.63%
Case 3	91.99%	93.89%	96.90%
Case 3(reconstructed)	92.47%	94.70%	97.24%
Case 4	92.09%	95.91%	95.44%
Case 4(reconstructed)	92.90%	95.91%	96.09%
Case 5	91.15%	96.33%	95.64%
Case 5(reconstructed)	91.58%	96.34%	95.75%

As shown in Table 6, under different class imbalance scenarios, the proposed reconstruction method consistently improves the classification performance of various models, demonstrating good generalization capabilities. For the traditional machine learning model, SVM, the classification accuracy is improved in all five imbalance cases after reconstruction, with improvements ranging from 0.43% to 0.91%. For the deep learning model, LSTM, a similar trend of stable performance gain can be observed in most cases. For example, in Cases 1 and 3, the classification accuracy increases from 94.42% to 95.13% and from 93.89% to 94.70%, respectively. The CNN model maintains a relatively high classification accuracy across all imbalance scenarios and further achieves consistent improvement after introducing reconstructed data. Specifically, in Case 1, the accuracy increases from 97.30% to 97.86%, and in Case 2, from 97.93% to 98.63%.

The improvement in classification accuracy across all models after dataset reconstruction indicates that the proposed method can effectively extract and reconstruct discriminative key features while preserving the intrinsic structural characteristics of the original signals, thereby enhancing sample quality and class separability.

Moreover, as the types of minority fault samples vary, the proposed method consistently improves classification performance under different conditions. This demonstrates that the method is not limited to specific fault types but is capable of unified modeling and reconstruction of power signals with diverse feature patterns. It further indicates that the proposed approach can effectively characterize multiple types of non-stationary features and achieve stable reconstruction across different feature distributions, thereby enhancing the adaptability of models under complex operating conditions.

4. Conclusions

We investigated non-stationary feature analysis and reconstruction methods for complex power signals characterized by a wide dynamic range, fast time variation, and strong randomness. The main contributions are summarized as follows.

(1) Based on our analysis of power equipment operating characteristics, three fundamental types of non-stationary features were identified, and a deterministic parametric model for quasi-periodic harmonics has been established. All model parameters are deterministic, enabling a more accurate analytical representation of apparently highly random signals.

(2) A high-resolution time–frequency representation framework is developed using a scaling-basis chirplet transform with four degrees of freedom, including time delay, scale, chirp rate, and center frequency. Combined with ridge detection, the instantaneous frequency and amplitude of signal components are effectively extracted and reconstructed, achieving precise characterization of non-stationary features.

(3) To address the difficulty of power signal acquisition, a signal reconstruction method that preserves inter-component relationships is proposed, enabling the expansion of non-stationary feature libraries for power signals.

Although this study is primarily motivated by power metering applications, the proposed modeling strategy and time–frequency analysis framework can also apply to related fields such as fault diagnosis and arc monitoring, where extraction and characterization of non-stationary electrical signal features are essential. Future work will focus on further enhancing the theoretical foundations and extending the practical applicability of the proposed methods.

Author Contributions: Conceptualization, Y.H. and J.Y.; methodology, Y.H.; software, Y.H.; validation, Y.H.; formal analysis, Y.H.; investigation, Y.H.; data curation, Y.H.; writing—original draft preparation, Y.H.; writing—review and editing, J.Y.; visualization, Y.H.; supervision, J.Y.; project administration, J.Y. All authors have read and agreed to the published version of the manuscript.

Funding: This paper was supported by the State Grid Science and Technology Project "Low-carbon and Reliable Urban Power Distribution System Demonstration Project" (2024ZD0800800).

Data Availability Statement: The original contributions presented in this study are included in the article. Further inquiries can be directed to the corresponding author.

Conflicts of Interest: The authors declare no conflicts of interest.

Abbreviations

The following abbreviations are used in this manuscript:

CT	Chirplet Transform
PCT	Polynomial Chirplet Transform
GLCT	General Linear Chirplet Transform
VSLCT	Velocity Synchronous Linear Chirplet Transform
SBCT	Scaling-Basis Chirplet Transform
SST	Synchro Squeezing Transform
MSST	Multisynchrosqueezing Transform
STFT	Short-Time Fourier Transform
ASTFT	Adaptive Short-Time Fourier Transform
CWT	Continuous Wavelet Transform
WVD	Wigner–Ville Distribution

PWVD	Pseudo Wigner–Ville Distribution
TFR	Time–Frequency Representation
PWM	Pulse Width Modulation
DC	Direct Current
PLL	Phase-Locked Loop
SNR	Signal-to-Noise Ratio
MSE	Mean Square Error
AC	Alternating Current
p.u.	Per Unit
FFT	Fast Fourier Transform
DC/DC	Direct Current to Direct Current Converter
TFD	Time–Frequency Distribution

References

1. Cai, Y.; He, Y.; Zhang, H.; Zhou, H.; Liu, J. Research on harmonic state-space modeling and calculation analysis of low-switching-frequency grid-connected inverter considering the impact of digitization. *IEEE Trans. Power Electron.* **2022**, *38*, 1003–1021. [CrossRef]
2. Ma, X.; Liao, Z.; Wang, Y.; Zhao, J. Fast dynamic phasor estimation algorithm considering DC offset for PMU applications. *IEEE Trans. Power Deliv.* **2023**, *38*, 3582–3593. [CrossRef]
3. Yuan, R.M.; Li, W.W.; Wang, G.X.; Liu, J.P.; Wang, X.W. Construction of run-length waveform sample library in amplitude domain of complex dynamic power signals. *Electr. Meas. Instrum.* **2025**, *62*, 92–98.
4. Zhao, F.; Zhu, T.; Li, Z.; Wang, X. Low-frequency resonances in grid-forming converters: Causes and damping control. *IEEE Trans. Power Electron.* **2024**, *39*, 14430–14447. [CrossRef]
5. Shklyarskiy, Y.; Hanzelka, Z.; Skamyin, A. Experimental study of harmonic influence on electrical energy metering. *Energies* **2020**, *13*, 5536. [CrossRef]
6. Jiao, D.X.; Yuan, R.M.; Zhang, Z.J.; Ju, H.J.; Xiang, H.J.; Wang, X.W. Analysis of the impact of rapidly changing electricity signal waveform modal on the dynamic error of DC electricity meter. *Electr. Meas. Instrum.* **2024**, *61*, 194–204. [CrossRef]
7. Duan, J.; Tang, Q.; Li, N.; Qiu, W.; Yao, W. Predictive Health Management of Smart Meters: Daily Measurement Error Forecasting Under Complex Environmental Conditions. *IEEE Trans. Smart Grid* **2025**, *16*, 2429–2438. [CrossRef]
8. Wang, X.W.; Li, S.; Yuan, R.M.; Jiao, D.X.; Ju, H.J.; Meng, J. Dynamic Electric Energy Reference Signal Modeling of the Fast-changing Waveform Mode of DC Charging Piles. *Power Syst. Technol.* **2025**, *49*, 759–770. [CrossRef]
9. Yang, T.; Yang, F.X.; Ye, Z.S. A New Measurement method for Supraharmonics Based on Dynamic Sampling and Compressed Sensing. *Proc. CSEE* **2023**, *43*, 6278–6288. [CrossRef]
10. Sun, Y.Y.; Ge, J.; Xu, Q.S.; Zhao, G.L.; Wang, T.X.; Li, Q.L. Decoupling Harmonic Contribution Evaluation Considering Multi-frequency Coupling Effects. *Proc. CSEE* **2025**, *45*, 8268–8281. [CrossRef]
11. Laadjal, K.; Sahraoui, M.; Cardoso, A.J.M. On-line fault diagnosis of DC-link electrolytic capacitors in boost converters using the STFT technique. *IEEE Trans. Power Electron.* **2020**, *36*, 6303–6312. [CrossRef]
12. Yan, Y.; Trinchero, R.; Stievano, I.S.; Li, H. Implementation of Adaptive Partial Discharge Denoising in Resource-Limited Embedded Systems via Efficient Time-Frequency Matrix Factorization. *IEEE Trans. Instrum. Meas.* **2024**, *73*, 3518213. [CrossRef]
13. Abouyehia, M.; Egea-Alvarez, A.; Aphale, S.S.; Ahmed, K.H. Novel frequency-domain inertia mapping and estimation in power systems using wavelet analysis. *IEEE Trans. Power Syst.* **2024**, *40*, 2557–2567. [CrossRef]
14. Jiang, T.; Liu, B.; Liu, G.; Wang, B.; Li, X.; Zhang, J. Forced oscillation source location of bulk power systems using synchrosqueezing wavelet transform. *IEEE Trans. Power Syst.* **2024**, *39*, 6689–6701. [CrossRef]
15. Ahmad, A.A.; Airoboman, A.E.; Abdulaziz, A.; Hussaini, H. Power quality disturbances analysis using two forms of Wigner-Ville distribution. In *2019 IEEE PES/IAS PowerAfrica*; IEEE: Abuja, Nigeria, 2019; pp. 424–428.
16. Zhong, J.; Huang, Y. Time-frequency representation based on an adaptive short-time Fourier transform. *IEEE Trans. Signal Process.* **2010**, *58*, 5118–5128. [CrossRef]
17. Wu, X.; Liu, T. Spectral decomposition of seismic data with reassigned smoothed pseudo Wigner–Ville distribution. *J. Appl. Geophys.* **2009**, *68*, 386–393. [CrossRef]
18. Hazra, B.; Narasimhan, S. Gearbox fault detection using synchro-squeezing transform. *Procedia Eng.* **2016**, *144*, 187–194. [CrossRef]
19. Yan, S.; Sun, Y. Early chatter detection in thin-walled workpiece milling process based on multi-synchrosqueezing transform and feature selection. *Mech. Syst. Signal Process.* **2022**, *169*, 108622. [CrossRef]
20. Mann, S.; Haykin, S. The chirplet transform: Physical considerations. *IEEE Trans. Signal Process.* **1995**, *43*, 2745–2761. [CrossRef]

21. Peng, Z.K.; Meng, G.; Chu, F.L.; Lang, Z.Q.; Zhang, W.M.; Yang, Y. Polynomial chirplet transform with application to instantaneous frequency estimation. *IEEE Trans. Instrum. Meas.* **2011**, *60*, 3222–3229. [CrossRef]
22. Yang, Y.; Peng, Z.K.; Meng, G.; Zhang, W.M. Spline-kernelled chirplet transform for the analysis of signals with time-varying frequency and its application. *IEEE Trans. Ind. Electron.* **2011**, *59*, 1612–1621. [CrossRef]
23. Yu, G.; Zhou, Y. General linear chirplet transform. *Mech. Syst. Signal Process.* **2016**, *70*, 958–973. [CrossRef]
24. Guan, Y.; Liang, M.; Necsulescu, D.S. Velocity synchronous linear chirplet transform. *IEEE Trans. Ind. Electron.* **2018**, *66*, 6270–6280. [CrossRef]
25. Maison, T.; Silva, F.; Bernardoni, N.H.; Guillemain, P. High-order chirplet transform for efficient reconstruction of multicomponent signals with amplitude modulated crossing ridges. *Signal Process.* **2025**, *231*, 109887. [CrossRef]
26. López, C.; Moore, K.J. Enhanced adaptive linear chirplet transform for crossing frequency trajectories. *J. Sound. Vib.* **2024**, *578*, 118358. [CrossRef]
27. Chui, K.C.; Mhaskar, H. Signal decomposition and analysis via extraction of frequencies. *Appl. Comput. Harmon. Anal.* **2016**, *40*, 97–136. [CrossRef]
28. Yen, Y.J.; Lu, D.Y.; Yeh, S.Y.; Ding, J.-J.; Shen, C.-Y. High-Order Synchrosqueezed Chirplet Transforms for Multicomponent Signal Analysis. *Appl. Comput. Harmon. Anal.* **2025**, *82*, 101839. [CrossRef]
29. Zhang, W.; Deng, Z.; Wu, T.; Jia, Z.; Xing, G.; Wang, Z.; Yan, C.; Luo, H. Self-correcting linear chirplet transform for the separation of signals with crossover frequencies. *Measurement* **2025**, *253*, 117492. [CrossRef]
30. Li, M.; Wang, T.; Chu, F.; Han, Q.; Qin, Z.; Zuo, M.J. Scaling-basis chirplet transform. *IEEE Trans. Ind. Electron.* **2020**, *68*, 8777–8788. [CrossRef]
31. Gong, T.; Wen, W.; Dong, Y.; Gao, Z.; Zhang, W. Nyström-Aware Approximations for Matrix-based Rényi's Entropy. *Neural Netw.* **2025**, *195*, 108268. [CrossRef]
32. Sun, Z.; Machlev, R.; Wang, Q.; Belikov, J.; Levron, Y.; Baimel, D. A public data-set for synchronous motor electrical faults diagnosis with CNN and LSTM reference classifiers. *Energy AI* **2023**, *14*, 100274. [CrossRef]